

Application of FEM in the assessment of phenomena associated with dynamic investigations on a miniaturised DICT testing stand

W. Moćko^{1,2*}, Z. L. Kowalewski^{1,2}

¹*Institute of Fundamental Technological Research, Pawińskiego 5B, 02-106 Warsaw, Poland*

²*Motor Transport Institute, Jagiellońska 80, 03-301 Warsaw, Poland*

Received 28 November 2011, received in revised form 28 May 2012, accepted 12 September 2012

Abstract

This paper presents the assembly of the miniaturised direct impact compression test method (MDICT) developed at the Institute of Fundamental Technological Research at the Polish Academy of Sciences (IFTR PAS). Additionally, this method was used to investigate the mechanical properties of tantalum at the strain rate of $8 \times 10^5 \text{ s}^{-1}$. To analyse the phenomena occurring during the tests, a numerical model of the testing stand was developed and validated. The finite element (FEM) model was expanded to estimate the sources of error achieved in the results using the analytical methods. The effects related to friction, inertia, specimen ratio, adiabatic heating, stress equilibration and strain rate on the stress-strain characteristic observed before and after the analytical correction were discussed.

Key words: miniaturised Hopkinson bar, tantalum, high strain rates, direct impact, finite element method

1. Introduction

The application of the miniaturised direct impact compression test method (MDICT) allows the investigation of the mechanical properties of materials at strain rates within the range of 10^4 s^{-1} to $1.5 \times 10^5 \text{ s}^{-1}$, which are higher than the normal strain rates reached by the split Hopkinson pressure bar (SHPB) method. The results of the MDICT tests may be applied to characterise the dynamic properties of materials at high strain rates in which viscous-drag effects must be considered [1, 2]. The presented methodology may be useful in many applications, such as the testing of impact protection structures, ballistic shields, bulletproof vests, helmets, turbines, and aeronautic/astronautic structures, as well as basic research concerning material properties.

Many unfavourable phenomena occur during MDICT experiments that may affect the experimental data, such as friction, inertia, adiabatic heating and mechanical wave dispersion. Because of the small dimensions of the testing stand and a very short test time, there is no practical way to use a high-speed camera during specimen deformation to validate the

results. Furthermore, the classical redundant methods of data acquisition (i.e., three-wave analysis and additional optical measurement of interface displacement) are also not suitable, because the incident bar is removed from the measuring track. The authors of the present study applied a finite element method model, developed in the ABAQUS environment, to investigate the MDICT test process. Moreover, the phenomena mentioned above and the analytical methods for correction were simulated and discussed.

2. MDICT testing stand

The idea of removing the incident bar from a typical SHPB [3] testing stand is called a DICT and was first presented in 1970 [4]. The basic advantage of this solution is that there is a significant increase in the calculated specimen strain rate, which is approximately V_0/l_0 . The miniaturised testing stand provides strain rates of up to $1.5 \times 10^5 \text{ s}^{-1}$ at a projectile velocity V_0 of 150 m s^{-1} , and an initial specimen length l_{S0} of 1 mm. The reduction in the specimen length also entails a reduction of its diameter to ensure the spe-

*Corresponding author: e-mail address: wmocko@ippt.gov.pl

cimen shape coefficient l_{S0}/d_{S0} is maintained at 0.5, which is necessary to minimise the frictional and inertial effects [5]. The decreased specimen dimensions require the overall testing stand dimensions to be reduced, which gives the following advantages:

- decreased time to attain homogeneous strain in a specimen;
- reduced deformation gradients due to elastic wave propagation along the compression direction;
- limited effects of the longitudinal and transversal inertia;
- decreased elastic dispersion of the longitudinal wave.

The main difficulty related to the MDICT method arises during an accurate measurement of the interface displacement. Various assumptions and apparatus were applied in previous experiments to estimate the displacement magnitude:

- the projectile is perfectly rigid [4];
- the velocity of the back side of the projectile was estimated [6];
- a high speed camera was used [7];
- a stress equilibrium state inside the specimen was assumed [7, 8].

Two problems occur during the displacement measurements using the MDICT. First, there is no incident bar, and consequently, the acquisition of the incident and reflected elastic waves is disabled. Second, the deformation process takes only several microseconds, which induces a minimal bandwidth of 10 MHz. To ensure that the accuracy of the displacement measurement is better than $\varepsilon = 0.01$, the resolution must be higher than 10 μm . Only a few solutions, based mainly on optical methods [9], have been described for the purpose of deformation measurements. One of those methods is known as the laser occlusive radius detector (LORD) [10]. The LORD uses the instantaneous diameter value to estimate the strain magnitude. A coherent parallel light beam is detected using a photo detector. A part of the light beam is shadowed by the specimen, which increases its diameter during deformation. Consequently, the width of the light beam reaching the detector decreases. Assuming a constant specimen volume during the plastic deformation, the strain waveform may be determined using the light intensity.

A two-channel optical extensometer [11] is another technique used to measure the displacement during the DICT tests. The optical extensometer is able to detect the displacement of the border between the light and dark areas. The transmitter bar and projectile are coated by black paint, and the specimen is coated by white paint. The first channel of the extensometer is used to determine the displacement of the projectile/specimen interface, while the second channel acquires the movement of the specimen/transmitter bar interface. The major limitation

of this method is that the lens' field of view is the specimen size, which must be greater than 3 mm.

The shadow principle method may also be applied to determine the MDICT measurements [1]. The working principle is similar to that of the LORD system; however, instead of measuring the specimen diameter, the distance between the projectile and the de-accelerator tube is determined. A coherent beam of light is partially shadowed by the projectile and the de-accelerator tube from either side. The amount of light acquired by the photo detector is proportional to the movement of the projectile with respect to the tube.

The available literature provides descriptions of miniaturised testing stands with a bar diameter of less than 5 mm, which are used to investigate the dynamic properties of aluminium, aluminium alloys, copper, iron and tungsten using the SHPB method [12, 13] and the direct impact method (DIM) [7, 8, 14]. The highest strain rates ($2.5 \times 10^5 \text{ s}^{-1}$) were achieved by Kamler [8] using a stand with a 1.5 mm diameter bar. Copper specimens with a length of 0.3 mm and a diameter of 0.7 mm were tested. The experiments presented in this report were performed using a new DICT stand design [1]. The diameter of the measuring bar was reduced to 3 mm [15, 16]. Tests were performed on the polycrystalline tantalum. The mechanical properties of tantalum are relatively well known in the range of static and dynamic loads up to 10^4 s^{-1} [17, 18]. However, limited data are available in the case of deformations at very high strain rates (above 10^4 s^{-1}). Such results have been obtained by Dupfrey and Clifton [19] using a pressure-shear plate impact at the strain rate of 10^6 s^{-1} . There are still no results obtained using the Hopkinson bar in the range of 10^4 s^{-1} to 10^5 s^{-1} .

The application of FEM is a promising alternative for experimental result validation, especially for the MDICT method. Selected examples of such an approach are cited in the references [20–23].

3. FEM model for the tests analysis on the MDICT

A diagram of the MDICT device, which allows the testing of mechanical properties of materials at very high strain rates, is shown in Fig. 1. The main part of the device is a transmitter bar (3) made of maraging steel with a diameter of 3 mm and length of 248 mm. To protect the bar from buckling, supporting teflon bearings (7) are spaced 40 mm apart along the bar. The elastic wave is absorbed by the damper (8) mounted at the end of the bar, while the radial bar oscillations are minimised by the radial damper (6). To acquire the elastic waveform, two strain gauges with a length of 0.6 mm (4) are confined symmetrically on

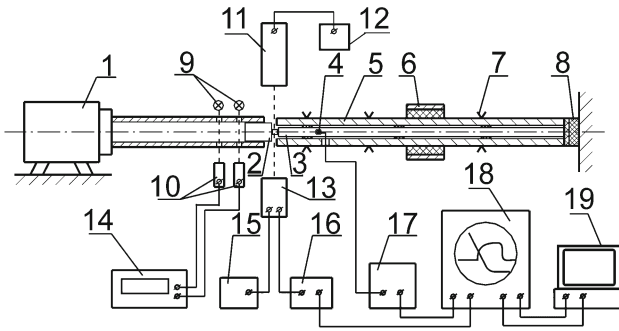


Fig. 1. Diagram of the MDICT: 1 – compressed air launcher, 2 – projectile, 3 – transmitter bar, 4 – strain gauge, 5 – de-accelerator tube, 6 – radial damper, 7 – support, 8 – damper, 9 – photodiodes, 10 – photo detectors, 11 – coherent laser light source, 12 – power supply, 13 – photo detector with lenses, 14 – time counter, 15 – power supply, 16 – amplifier, 17 – SG bridge circuit, 18 – digital oscilloscope, 19 – PC computer.



Fig. 2. A view of the MDICT testing stand developed at IFTR PAS.

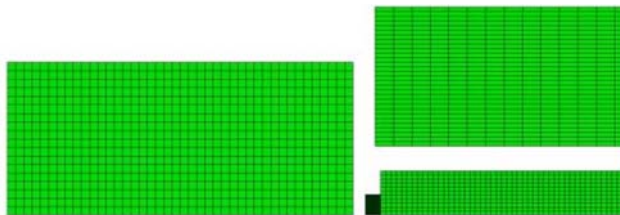


Fig. 3. The FEM model of the MDICT testing stand.

the bar at a distance of 22 mm from the specimen/bar interface. The gauges are connected in serial to prevent bending influence on the results. The signal from the gauges is amplified using a wideband bridge circuit (17) and stored using a digital oscilloscope (18) for further analysis (19). The projectile (2) with a diameter of 11 mm and length of 12.5 mm is made of maraging

steel and may be accelerated in a pneumatic launcher (1) within a range of velocities of 20 m s^{-1} to 150 m s^{-1} . The projectile hits the tested specimen and induces its plastic deformation until the projectile movement is stopped by the de-accelerator tube (5), which can be drawn out over the transmitter bar within a distance of 0 to 1 mm. This type of solution prevents the transmitter bar from undergoing plastic deformation and allows specimen recovery after a given strain to then undergo further analysis, e.g., microstructural. The photo of the testing stand is shown in Fig. 2.

Simulations were carried out using the software ABAQUS/Explicit 6.11. The total number of elements and nodes was 5155 and 5835, respectively. The mesh size was 0.15 mm for the transmitter bar, 0.4 mm for the striker and 0.03 mm for the specimen. More information about FEM modelling of a MDICT may be found in previous studies [24, 25].

The FEM model (Fig. 3), including the basic elements of the device (i.e., the projectile, transmitter bar, de-accelerator tube and specimen), was developed for the purpose of numerical analysis. The shape, dimensions and location of the particular parts of the model correspond to the real testing stand. Boundary conditions for the model were set in the following way:

- two-axis confinement of the mounting surface of the transmitter bar and the de-accelerator tube;
- initial temperature of the specimen was 298 K;
- no heat exchange through the specimen interfaces;
- initial velocity of the projectile was 55 m s^{-1} .

The axisymmetric model was used to investigate the influence of the adiabatic heating, the specimen ratio and various friction coefficients (0, 0.1 and 0.2) on the results. It was assumed that all parts of the testing stand were made of maraging steel with Young's modulus, E_S , equal to 200 GPa and density, ρ_S , of 7860 kg m^{-3} .

The FEM-based stress-strain curves were obtained using the same computer application and input data as the experiment. To obtain the required data for the analysing software, displacement of the striker face and the axial stress in the transmitter bar were evaluated 22 mm from the interface. More information about FEM modelling of a MDICT may be found in previous studies [24, 25].

The stress-strain characteristics of the polycrystalline tantalum, used as the specimen material, were calculated based on the Zerilli-Armstrong constitutive equation for the BCC materials [26]:

$$\sigma = c_0 + B_0 e^{-(\beta_0 - \beta_1 \ln \dot{\epsilon})T} + K \epsilon^n. \quad (1)$$

The coefficients were determined in previous studies [18], i.e., $c_0 = 30 \text{ MPa}$, $B_0 = 1125 \text{ MPa}$, $\beta_0 = 0.00535 \text{ K}^{-1}$, $\beta_1 = 0.000327 \text{ K}^{-1}$ and $n = 0.44$.

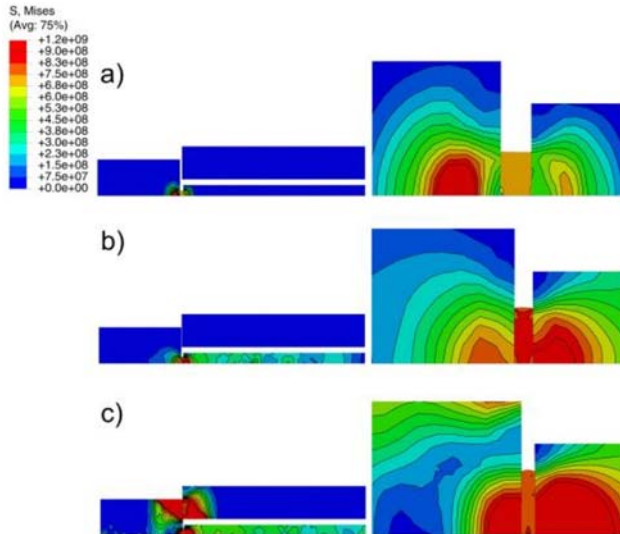


Fig. 4. Distribution of the von Mises stress inside the specimen and parts of the testing stand for a frictional coefficient $\mu = 0.1$ and specimen dimensions: $l_0 = 0.55$ mm and $D_0 = 1.5$ mm during the following stages of the experiment: (a) $t = 8.4$ μs , (b) $t = 13.4$ μs , (c) $t = 15.9$ μs . The distribution is determined using FEM analysis.

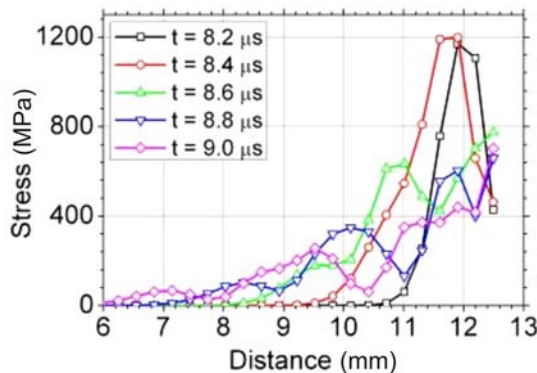


Fig. 5. Huber-Mises stress along the striker axis in the subsequent stages after specimen impact.

The subsequent stages of specimen deformation are presented in Fig. 4. Figure 4a shows the state of contact between projectile and specimen in the initial stage of attaining stress equilibrium. The area of high stress can be observed inside the projectile near the interface and inside the transmitter bar. There is a magnitude decrease in the stress with an increase of distance to the interface. A distribution of stress during the plastic deformation of the specimen is illustrated in Fig. 4b. The process of elastic wave propagation takes place inside the projectile and the transmitter bar. The axial stress distribution in the cross-section is strongly inhomogeneous near the interface. The stress distribution improves for sections

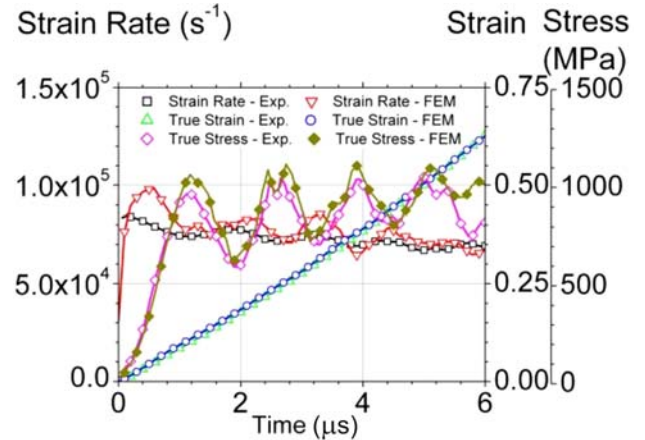


Fig. 6. Comparison of the waveforms obtained using the MDICT experiment and the FEM calculations.

placed further away from the interface. According to current knowledge [1], the stress distribution may be considered homogeneous for the sections located further from the interface by a distance calculated as the bar diameter multiplied by a factor of 5. Figure 4c shows the process of the projectile stopping in the de-accelerator tube. Because of the elastic properties of the tube material, the braking time takes non-zero values. Hence, despite the strain rate decrease, the specimen is still being deformed for a short time. This is important because the approach is to use a pre-strained specimen followed by a microstructural investigation. Because of the projectile impact, an elastic wave is generated inside the de-accelerator tube; however, this wave does not significantly disturb the results.

The pulse of the high magnitude stress is generated during striker impact on the specimen. Development of the stress inside the striker at subsequent time intervals after impact is shown in Fig. 5. It can be observed that this pulse propagates along the striker axis while the stress decreases by a magnitude relative to the distance from the striker/specimen interface. The probable reason of such behaviour may be the inertia of the specimen material or the Pochhammer-Chree vibrations in the striker.

Figure 6 shows the comparison between the experimental results and the calculated results. Both curves show good agreement with respect to shape and magnitude:

- the strain rate decreases from a value of $8 \times 10^4 \text{ s}^{-1}$ to $7.5 \times 10^4 \text{ s}^{-1}$ at $6 \mu\text{s}$ of the test;
- the characteristics of the strain waveforms are very similar and the magnitude of the strain is $\varepsilon = 0.65$ at $6 \mu\text{s}$ of the test;
- the experimental and calculated stress waveforms are comparable. Moreover, strong oscillations of the same amplitude and period are superimposed on both the curves.

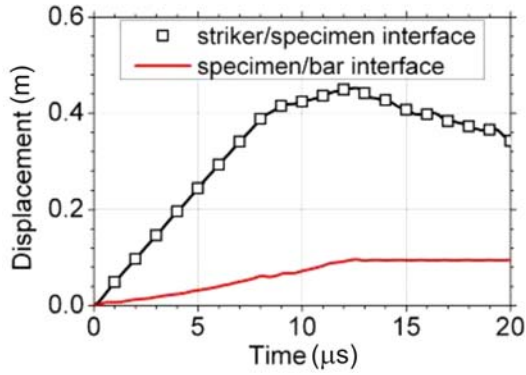


Fig. 7. Displacement of the projectile/specimen and specimen/bar interfaces during the test determined using FEM analysis.

It can be concluded from the preliminary investigation that the results obtained using the MDICT methodology are in reasonable agreement with the FEM simulation. Therefore, the numerical analysis can be applied to investigate the particular phenomena during the MDICT experimental investigation.

4. An analysis of fast specimen deformation

4.1. Deformation rate

A theoretical strain rate was determined for both the perfectly rigid projectile and the transmitter bar. It was found to be $\dot{\epsilon} = 10^5 \text{ s}^{-1}$ under the following assumptions: constant velocity of the projectile $V_0 = 55 \text{ m s}^{-1}$, and initial length of the specimen $l_{s0} = 0.55 \text{ mm}$. Experimental data shows, however, that the strain rate decreases with an increase of the strain magnitude from $\dot{\epsilon} = 0.8 \times 10^5 \text{ s}^{-1}$ to $\dot{\epsilon} = 0.7 \times 10^5 \text{ s}^{-1}$. This is because the transmitter bar is deflected during the plastic deformation of the specimen, as shown in Fig. 7. A displacement of the projectile/specimen interface can be treated as a linear process, and consequently, the assumption that the projectile has a constant velocity during the test may be validated. The projectile stopping after impact to the de-accelerator tube takes place between 7 to 12 μs of the experiment. The specimen/bar interface moves with an increasing velocity. A plastic deformation of the specimen results in an increase in the contact area between specimen and bar. Therefore, the force deflected in the interface increases as well.

The main task of the Hopkinson bar test is to determine the stress-strain curve of the tested material at the strictly defined strain rate. This test requires a constant, true strain rate to be maintained during the plastic deformation process. In this case, the true strain rate is defined as $d\varepsilon_T(t)/dt$, where $\varepsilon_T(t)$ is the

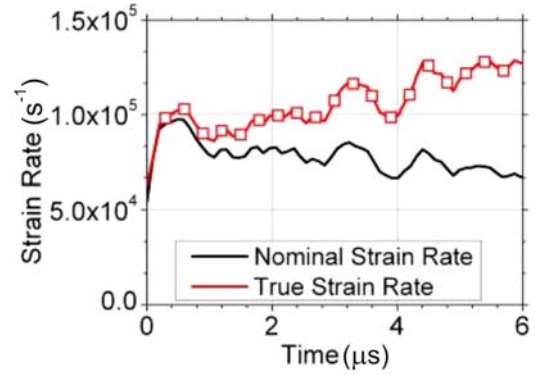


Fig. 8. Nominal and true strain rates found using FEM analysis.

true strain. The true strain rate value increases from $\dot{\epsilon} = 0.8 \times 10^5 \text{ s}^{-1}$ to $\dot{\epsilon} = 1.2 \times 10^5 \text{ s}^{-1}$ at the end of test (Fig. 8). Applying the ZA model for tantalum, it is estimated that an increase in the flow stress, which is related to the strain rate hardening due to the non-constant true strain rate, equals 3 % at a strain of 0.6.

4.2. Adiabatic heating

The process of adiabatic heating is related to the transformation of plastic deformation work into heat. Because of the adiabatic conditions, the flow stress decreases with an increase in the deformation level. The instabilities, in the form of adiabatic shear bands (ASB), may appear at high strain magnitudes [27–29]. The instabilities can lead to the material being damaged. It is assumed that for the strain of $\dot{\epsilon} < 10 \text{ s}^{-1}$, the deformation process is isothermal, whereas for higher rates, it becomes adiabatic. To compare the stress-strain characteristics obtained at a high strain rate with static conditions, dynamic curves must be corrected into the isothermal conditions [27]. An increase of the temperature due to plastic work during specimen deformation can be expressed in the following way:

$$\Delta T = \frac{\beta}{\rho(T_0) C_v(T_0)} \int_0^{\varepsilon_{pm}} \delta[\varepsilon_p, \dot{\varepsilon}_p(\varepsilon_p), T_0] d\varepsilon_p, \quad (2)$$

where β is Taylor-Quinney's coefficient (usually assumed as 0.9), ρ is material density (16690 kg m^{-3}), C_v is heat capacity ($140 \text{ J kg}^{-1} \text{ K}^{-1}$) and T_0 is initial temperature (298 K).

Figure 9 shows the comparison between the calculated stress-strain characteristics of tantalum for the adiabatic and reference isothermal conditions. The

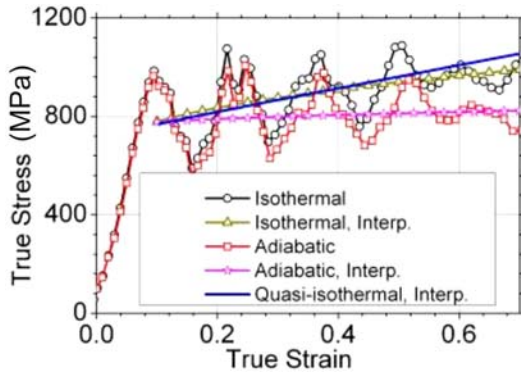


Fig. 9. The influence of adiabatic heating on the stress-strain characteristic determined using FEM analysis.

chart also includes curves averaged by the power-law

function (3) to help the results analysis:

$$\sigma(\varepsilon) = A + B\varepsilon^n. \quad (3)$$

A softening effect due to the temperature increase (~ 150 K) during the plastic deformation induces essential discrepancies between the stress-strain curves obtained under adiabatic and isothermal conditions. The difference between both curves increases with the strain level. For example, at $\varepsilon = 0.5$ the difference equals 130 MPa, which corresponds to 14 % in the relative units. The adiabatic curve is corrected to the isothermal conditions using Eq. (2) and is presented in Fig. 9. The difference in the flow stress is reduced significantly, up to 20 MPa at $\varepsilon = 0.5$ (2 % in the relative units). It can be concluded that the method of adiabatic heating correction gives relatively accurate results; however, this method requires basic knowledge

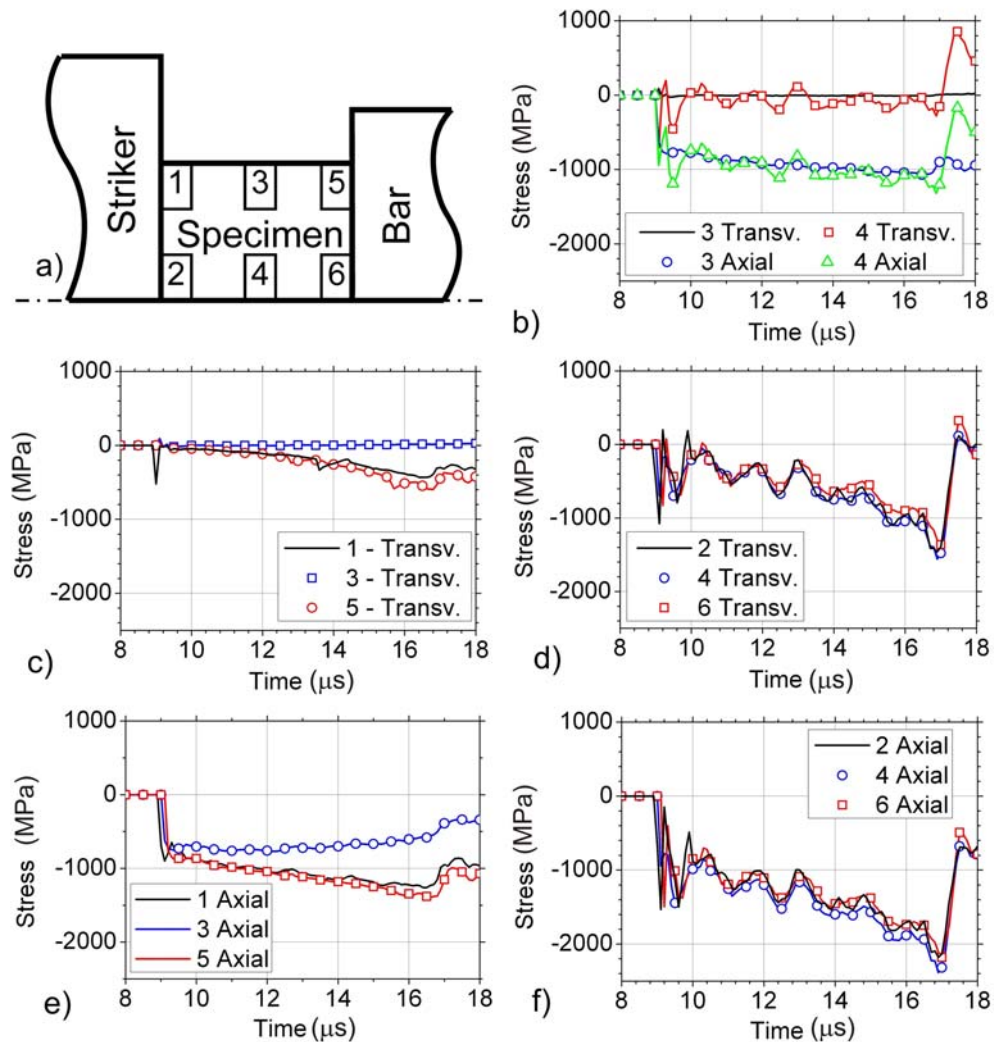


Fig. 10. Stress components inside the specimen during compression as found through FEM analysis: (a) arrangement of areas, (b) stress at zero-friction conditions, (c)–(f) stress at friction coefficient $\mu = 0.1$.

about the dependence between flow stress and temperature. These characteristics can be easily determined with the use of the SHPB testing stand equipped with the temperature chamber.

The step loading method [30] is another method used for the adiabatic heating effects reduction. The specimen is loaded with sequences of single pulses inducing a limited amount of deformation. Between each sequence, the specimen is conditioned to return to the initial temperature. The procedure is repeated until the strain magnitude reaches the chosen value. To obtain the entire stress-strain curve under quasi-isothermal conditions, the first few points of the adiabatic curves are taken into account and linked together. Confinement of the loading pulse can be achieved using various specimen recovery methods that rely on stopping the loading pulse or damping the reflected mechanical waves; therefore, only the first wave causes a deformation of the specimen. Specimen recovery is a desirable technique. This technique allows to re-use specimens in subsequent tests, such as experiments containing pulse loading or microscopic investigations assessing structural effects. In the MDICT presented here, the step loading method was not taken into account due to the small dimensions of the specimen, which cause large technical problems when the specimen is placed at the transmitter bar interface.

4.3. Frictional effects

An increase in the frictional coefficient at the specimen interface induces complex stress state inside the specimen; consequently, there is an overestimation of the flow stress. The influence of the friction on the axial and transversal component of the stress is presented in Fig. 10. The analysis was carried out in 6 areas; these locations are shown in Fig. 10a. The fields denoted as 2, 4 and 6 were distributed along the specimen axis, while those denoted as 1, 3 and 5 were on the specimen perimeter.

Stress variations versus time for the reference conditions (zero friction) are presented in Fig. 10b. It should be emphasised that due to the negligible differences between the curves for areas 1, 3, 5 and 2, 4, 6, redundant data were omitted.

The following conclusions could be drawn based on the analysis of the frictionless case:

- The magnitude of the transversal stress component is negligible near the specimen axis (area 4) as well as on the specimen perimeter (area 3).
- A curve representing the axial stresses component inside area 3 and 4 is of the same shape as a stress-strain characteristic of the applied tantalum constitutive model.
- Strong oscillations are present inside the specimen axis (area 4).

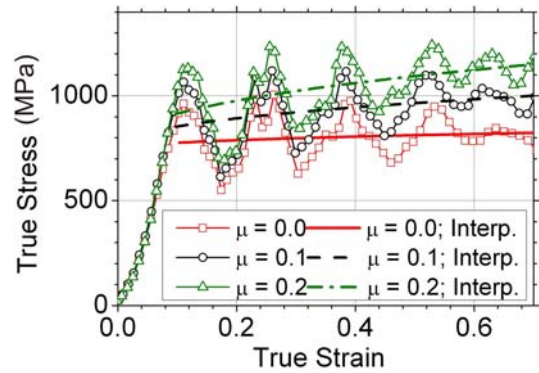


Fig. 11. The influence of frictional effects on the flow stress, as found by FEM analysis.

The results achieved for the frictional coefficient $\mu = 0.1$ are shown in Fig. 10 c–f. Furthermore, conclusions in this case are as follows:

- The magnitude of the transversal stress component is equal to zero for the 3rd area. It is similar to the frictionless conditions; however, near the interfaces (area 1 and 5), the stress magnitude increases with strain level.
- The magnitude of the transverse stress component near the specimen axis increases with the plastic strain value; moreover, the curve is characterised by strong oscillations.
- The magnitude of the axial stress component on the specimen perimeter is similar to that being under frictionless conditions at the beginning of the deformation process. However, in area 3, stress begins to decrease with an increase of the plastic strain. In contrast, the stress value at frictional condition increases more than during the frictionless conditions inside the areas 1 and 5.
- The magnitude of the axial stress component near the specimen axis (areas 2, 4 and 6) increases more than it does under the frictionless conditions.
- The analysis was carried out for a friction coefficient equal to 0.1; thus, during plastic deformation, the specimen outer edge is rounded (Fig. 4). Therefore, an axial stress component on the deflected edge is smaller in the middle of specimen than near the interfaces. For frictionless conditions (Fig. 9b), axial stress measured at the specimen outer edge is independent of the distance from the interfaces.

An influence of the friction coefficient value on the stress-strain characteristic is illustrated in Fig. 11 for frictional coefficients of 0, 0.1 and 0.2 [31]. An increase of the friction causes an increase of the flow stress measured using the SHPB method.

An application of a special lubricant between the interfaces is one of the most popular solutions to minimise friction, and consequently, reduce errors due to friction. The lubricant also takes the role of the glue,

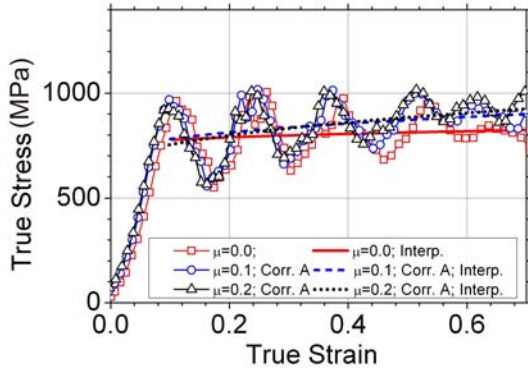


Fig. 12. Correction of the influence of friction on the stress-strain characteristic using Eq. (4), which is found through FEM analysis.

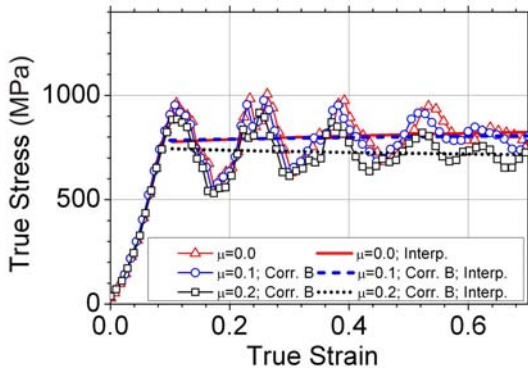


Fig. 13. Correction of the stress-strain characteristic reflecting the friction effect using Eq. (5), which is found through FEM analysis.

which enables better specimen positioning with respect to the transmitter bar surface. According to Eq. (4), an influence of friction on the flow stress can be reduced by increasing the specimen ratio. It should be mentioned, however, that increasing the specimen length decreases the strain rate for the given testing conditions. The decrease of strain rate is an undesirable phenomenon for this case. An influence of friction on the flow stress at the interfaces can be expressed analytically [32] using the following relationship:

$$\bar{\sigma} - \sigma = \frac{1}{3} \frac{\mu \bar{\sigma}}{s}, \quad (4)$$

where $\bar{\sigma}$ and σ are the mean values of the stress determined during the experiment and the true flow stress of the tested material, respectively, μ is the Coulomb friction coefficient and s is the transient specimen shape coefficient, which is the ratio between the length and diameter ($s = l/D$).

Using Eq. (4), the results can be corrected into the frictionless state, as presented in Fig. 12. This method

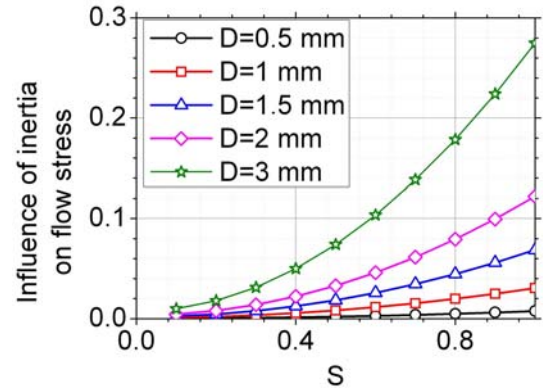


Fig. 14. Dimensionless measure of the inertia effect on flow stress.

underestimates the influence of friction on the stress curve, independently of the friction coefficient being analysed. The difference between true and measured stress increases with an increase of the plastic deformation from the start of the process at 0 MPa to 80 MPa at a strain $\varepsilon = 0.5$.

Another approach for minimising the friction effect has been reported in previous studies [33]. The following relationship has been proposed:

$$\bar{\sigma} = \frac{\sigma}{1 - \frac{\mu}{3s} \exp\left(\frac{3}{2}\varepsilon\right)}. \quad (5)$$

The results of the correction using Eq. (5) are shown in Fig. 13. The proposed method gives a good result for the friction coefficient $\mu = 0.1$. However, it overestimates the flow stress magnitude in the case of the friction coefficient $\mu = 0.2$. Interface lubrication is usually applied during experiments carried out on the MDICT; hence, the friction coefficient value is less than 0.1 [31]. Therefore, Eq. (5) was selected to correct the results.

4.4. Inertial effects

A difference between the measured and true magnitudes of the flow stress was observed due to the inertial effects and can be described using the following equation [34]:

$$\bar{\sigma} - \sigma = \rho D^2 \dot{\varepsilon}^2 \left(\frac{1}{64} + \frac{1}{6} s^2 \right) - \rho D^2 \dot{\varepsilon} \left(\frac{1}{32} - \frac{1}{6} s^2 \right) - \frac{\rho l \dot{v}}{2}, \quad (6)$$

where ρ is the density and v is the velocity of the specimen/bar interface. An error caused by inertia was calculated using Eq. (6) for various initial specimen diameters and dimension ratios and is depicted in Fig. 14. The following parameter values, obtained based on the experiment, were applied: $\dot{\varepsilon} = 8 \times 10^4 \text{ s}^{-1}$, $\dot{\varepsilon} = 2 \times 10^9 \text{ s}^{-2}$, $\rho = 1.7 \times 10^4 \text{ kg m}^{-3}$ and $D = 1.5 \text{ mm}$.

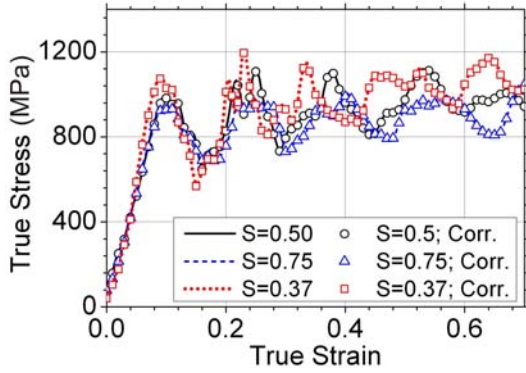


Fig. 15. The influence of inertia on the stress-strain characteristics, as found by FEM analysis.

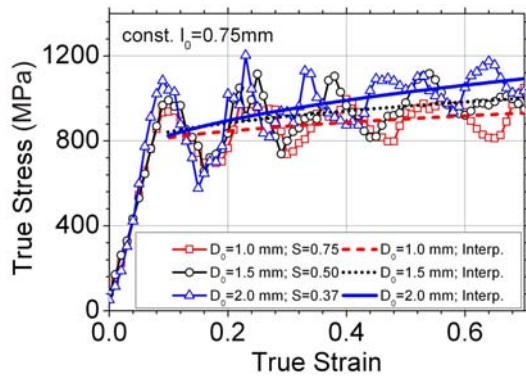


Fig. 16. The influence of the initial diameter on the stress-strain curve, as found by FEM analysis.

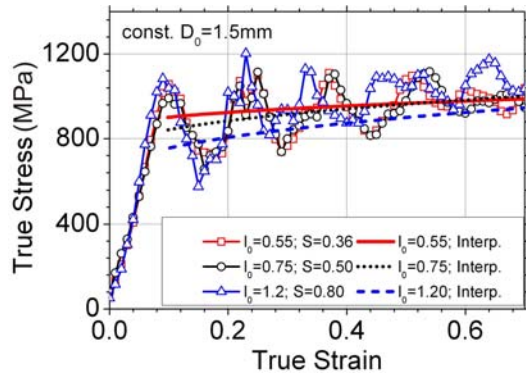


Fig. 17. The influence of the initial length on the stress-strain curve, as found by FEM analysis.

4.5. Specimen dimensions

The specimen dimensions directly influence the measured flow stress due to friction (Eqs. (4) and (5)) and inertial effects (Eq. (6)). However, in the following section, special attention is given to the gener-

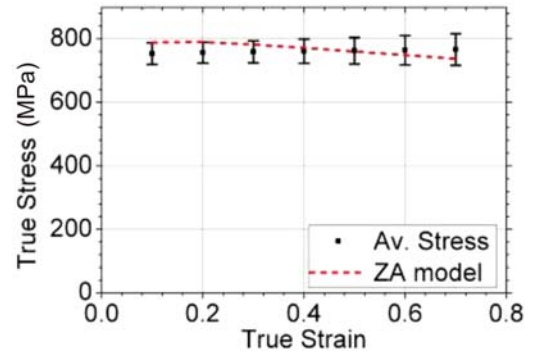


Fig. 18. The influence of the specimen geometry on the final flow stress. The data are averaged for 6 specimen ratios in comparison with the ZA model. This is shown by FEM analysis.

ation of the oscillations superimposed on the stress-strain curve (Fig. 15). The goal of the analysis was to estimate the flow stress measurement error induced by both the varied specimen dimension ratio and the curve interpolation (Eq. (3)). Six cases were simulated to investigate the oscillations caused by the dispersion effects [35, 36] with the following parameter:

l_0 – a constant length of 0.75 mm with various diameters of 1.0, 1.5 and 2.0 mm (Fig. 16);

D_0 – a constant diameter of 1.5 mm with various lengths of 0.55, 0.75 and 2.0 mm (Fig. 17).

The results were then corrected to frictionless conditions using Eq. (5), and the calculated curves were interpolated and averaged. A mean standard deviation was calculated based on six characteristics to assess the flow stress variation. The magnitude of the mean standard deviation was equal to 40 MPa, i.e., 5 % in relative units. The numerical results were compared with the ZA model predictions in Fig. 18. It could be concluded, that the ZA data are within the 5 % range around the mean value obtained for the 6 various specimen geometries; thus, the flow stress measurement error is less than 5 %.

4.6. Stress balancing process

An elastic mechanical wave propagates along a solid body with a velocity calculated from the following equation:

$$c_0 = (E/\rho)^{1/2}, \quad (7)$$

where c_0 is the elastic wave velocity, E is the Young's modulus, and ρ is the material density.

The velocity of the elastic wave for the tantalum is $c_0 = 3300 \text{ m s}^{-1}$. The time of wave propagation between interfaces is estimated analytically using Eq. (7) and determined to be $0.2 \mu\text{s}$, with the assumption

Table 1. Assessment of parameters and phenomena influencing the flow stress

	Impact on the final results at $\varepsilon = 0.5$ and $\mu = 0.1$	
	Raw data	Corrected
Strain rate	3 %	–
Inertial effects	1 %	0 %
Specimen dimension ratio	5 %	–
Stress balancing	$t > 1 \mu\text{s}$	–
Adiabatic heating	16 %	2 %
Friction	20 %	1 %

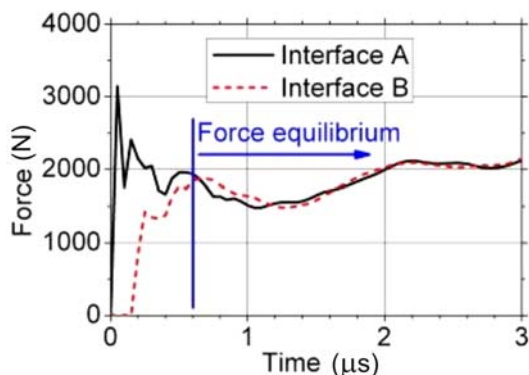


Fig. 19. Stress balancing in the specimen for the regions shown in Fig. 10a, using FEM analysis.

of a specimen length equal to 0.55 mm. Typically, the time required to obtain stress equilibrium takes about three multiples of the wave propagation [32]. Figure 19 shows the contact force recorded on both specimen interfaces with a time marked at 0.6 μs as the beginning of force equilibrium, according to Siebel's assertion [32]. As shown in Fig. 19, the condition of force equilibrium is satisfied 0.6 μs after the time of impact.

5. Discussion and concluding remarks

An influence of the phenomena evaluated based on the stress-strain characteristics of tantalum is summarised in Table 1. The analytical solution was applied to reduce the influence of friction, inertia and adiabatic heating effects on the experimental data. The following aspects were taken into account:

- The reduction of both the testing stand and specimen dimensions lead to limitations of the inertial effect. A magnitude of the flow stress error due to inertia is equal to 1 % despite the very high strain rate of $8 \times 10^4 \text{ s}^{-1}$. Furthermore, errors caused by the inertial effect were negligible after applying the analytical correction given by Eq. (6).

- The correction of the strong adiabatic heating effects using Eq. (2) enabled a reduction of the error

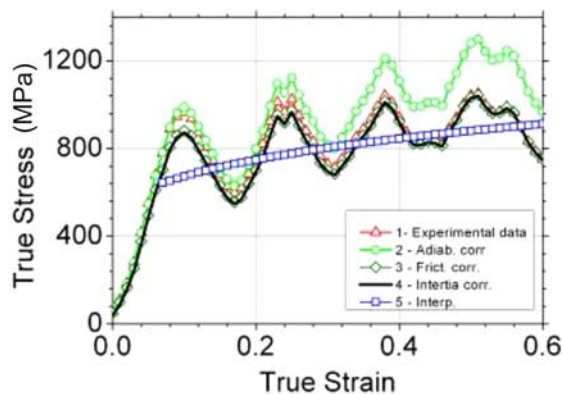


Fig. 20. The stress-strain curve for tantalum obtained using the MDICT before and after correction, as found experimentally.

magnitude from 16 % to 2 %.

- The friction induced an increase of the measured flow stress of approximately 20 %. However, an application of the second correction method (Eq. (5)) confined the strengthening effect up to 1 %. The application of a lubricant between contact surfaces diminishes the friction coefficient close to 0.1 [31]. Hence, it was assumed that the friction coefficient should be equal to 0.1.

- An influence of the strain rate variation on the flow stress during the plastic deformation process was investigated using specimens of length equal to 0.55 mm and a diameter of 1.5 mm. An increase of the true strain rate caused the 3 % increase of the flow stress at the level of deformation equal to 0.6.

- The time required to obtain a stress equilibrium state depends on the sound wave velocity, type of material and specimen length. A part of the curve corresponding to the stress balancing process, which relates to the process of stress equilibration, must be excluded from further analysis.

- A discrepancy between the ZA model and the numerical results for six various specimen dimension ratios was less than 5 % despite the strong oscillations (20 %).

The subsequent stages of experimental data correction using the method discussed are presented in

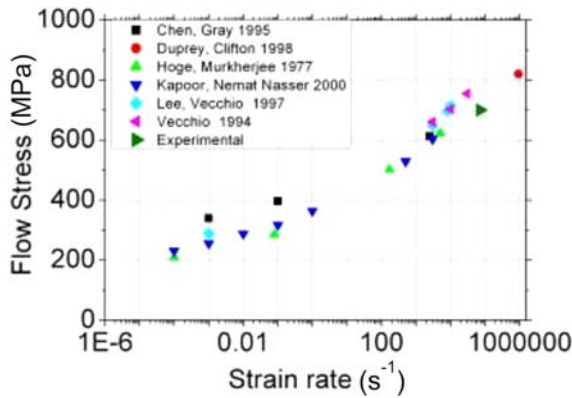


Fig. 21. Comparison of strain rate sensitivity of the tantalum based on our own data and previously reported results [17, 37–41].

Fig. 20. The MDICT results for the tantalum were corrected to capture effects of adiabatic heating, friction and inertia. Afterwards, the data were interpolated using a power-law function (Eq. (3)). The results of strain rate sensitivity were compared to the reference data in Fig. 21. It can be concluded that the experimental results are in good agreement with the other researchers' results. Furthermore, it should be emphasised that the present study shows stress-strain curves of the tantalum obtained with the use of Hopkinson bar method. Additionally, the highest strain rate for the tantalum was achieved in this study, when compared to previous Hopkinson bar experiments. Higher rates were only obtained when using other techniques [19]. By summarising the present work, the following conclusions could be drawn:

- The FEM model of the MDICT method was developed and applied to investigate phenomena taking place during specimen deformation. The model was previously validated by comparison with the experimental results.

- The analytical methods used to minimise the flow stress errors due to inertia, friction and adiabatic heating effects were analysed in terms of their application to the polycrystalline tantalum results. These methods are presented in the references. It may be concluded that the method originally developed for a normal size Hopkinson bar can also be used with MDICT methods at strain rates higher than 10^4 s^{-1} .

- An estimation of the stress-strain curve of the material tested is possible despite strong oscillations. A form of the applied equation can be elaborated by fitting the results of static tests or SHPB.

References

- [1] Malinowski, J. Z., Klepaczko, J. R., Kowalewski, Z. L.: *Exp. Mech.*, 47, 2007, p. 451. [doi:10.1007/s11340-006-9007-7](https://doi.org/10.1007/s11340-006-9007-7)
- [2] Rusinek, A., Rodriguez-Martinez, J. A.: *Mater. Design*, 30, 2009, p. 4377. [doi:10.1016/j.matdes.2009.04.011](https://doi.org/10.1016/j.matdes.2009.04.011)
- [3] Kolsky, H.: *Proc. Phys. Soc. B*, 62, 1949, p. 647. [doi:10.1088/0370-1301/62/11/302](https://doi.org/10.1088/0370-1301/62/11/302)
- [4] Dharan, C. M., Hauser, F. E.: *Exp. Mech.*, 10, 1970, p. 370. [doi:10.1007/BF02320419](https://doi.org/10.1007/BF02320419)
- [5] Malinowski, J. Z., Klepaczko, J. R.: *Int. J. Mech. Sci.*, 28, 1986, p. 381. [doi:10.1016/0020-7403\(86\)90057-3](https://doi.org/10.1016/0020-7403(86)90057-3)
- [6] Wulf, G. L.: *Int. J. Mech. Sci.*, 20, 1978, p. 609. [doi:10.1016/0020-7403\(78\)90019-X](https://doi.org/10.1016/0020-7403(78)90019-X)
- [7] Gorham, D. A.: *Inst. Phys. Conf. Ser.*, 47, 1980, p. 16.
- [8] Kamler, F., Niessen, P., Pick, R. J.: *Can. J. Phys.*, 73, 1995, p. 295. [doi:10.1139/p95-041](https://doi.org/10.1139/p95-041)
- [9] Michalíková, M., Ambriško, L., Pešek, L.: *Kovove Mater.*, 49, 2011, p. 137.
- [10] Ramesh, K. T., Narasimhan, S.: *Int. J. Solids Struct.*, 33, 1996, p. 3723. [doi:10.1016/0020-7683\(95\)00206-5](https://doi.org/10.1016/0020-7683(95)00206-5)
- [11] Klepaczko, J. R.: In: *New experimental methods in material dynamics and impact*. Warsaw, Inst. Fund. Technological Res., Polish Academy of Sciences 2002.
- [12] Lindholm, U. S.: In: *High Velocity Deformation of Solids*. Berlin, Springer-Verlag 1978.
- [13] Follansbee, P. S., Regazzoni, G., Kocks, U. F.: *Inst. Phys. Conf. Ser.*, 70, 1984, p. 71.
- [14] Shioiri, J., Sakino, K., Santoh, S.: In: *High/Very High Strain Rates*. Berlin, Springer-Verlag 1995.
- [15] Malinowski, J. Z.: *Developing of experimental method of investigation of viscoplastic metal properties at very high strain rates*. Warsaw, Inst. of Fund. Techn. Research, Polish Academy of Science 2010.
- [16] Moćko, W., Kowalewski, Z. L.: *Eng. Trans.*, 59, 2011, p. 235.
- [17] Hoge, K. G., Mukherjee, A. K.: *J. Mater. Sci.*, 12, 1977, p. 1666. [doi:10.1007/BF00542818](https://doi.org/10.1007/BF00542818)
- [18] Zerilli, F. J., Armstrong, R. W.: *J. Appl. Phys.*, 68, 1990, p. 1580. [doi:10.1063/1.346636](https://doi.org/10.1063/1.346636)
- [19] Duprey, K. E., Clifton, R. J.: In: *Shock compression of condensed matter*. Melville, NY: American Institute of Physics 1998, p. 475.
- [20] Sasso, M., Newaz, G., Amodio, D.: *Mat. Sci. Eng. A*, 487, 2008, p. 289. [doi:10.1016/j.msea.2007.10.042](https://doi.org/10.1016/j.msea.2007.10.042)
- [21] Ramirez, H., Rubio-Gonzalez, C.: *Mater. Design*, 27, 2006, p. 2736.
- [22] Jankowiak, T., Rusinek, A., Lodygowski, T.: *Finite Elem. Anal. Des.*, 47, 2011, p. 1191. [doi:10.1016/j.finel.2011.05.006](https://doi.org/10.1016/j.finel.2011.05.006)
- [23] Li, F., Chu, G. N., Lin, J. F., Feng, S. I.: *Kovove Mater.*, 48, 2010, p. 233.
- [24] Moćko, W., Kowalewski, Z. L.: *Transport Samochodowy*, 32, 2011, p. 97.
- [25] Moćko, W., Kowalewski, Z. L.: In: *Proceedings of the 28th Danubia-Adria-Symposium on Advances in Experimental Mechanics*, 2011, p. 119.
- [26] Zerilli, F. J., Armstrong, R. W.: *J. Appl. Phys.*, 61, 1987, p. 1816. [doi:10.1063/1.338024](https://doi.org/10.1063/1.338024)
- [27] Klepaczko, J. R., Duffy, J.: *Strain Rate History Effects in Body-Center-Cubic Metals*. ASTM-STP 765, No. 251, 1982.
- [28] Klepaczko, J. R.: *Int. J. Mech. Sci.*, 10, 1968, p. 297. [doi:10.1016/0020-7403\(68\)90014-3](https://doi.org/10.1016/0020-7403(68)90014-3)
- [29] Semiatin, S. L., Jonas, J. J.: *Formability and Workability of Metals*. Metals Park, Ohio, ASM 1984.

- [30] Nemat-Nasser, S., Li, Y. F., Isaacs, J. B.: *Mech. Mater.*, 17, 1994, p. 111.
[doi:10.1016/0167-6636\(94\)90053-1](https://doi.org/10.1016/0167-6636(94)90053-1)
- [31] Hartley, R. S., Cloete, T. J., Nurick, G. N.: *Int. J. Impact Eng.*, 10, 2007, p. 1705.
[doi:10.1016/j.ijimpeng.2006.09.003](https://doi.org/10.1016/j.ijimpeng.2006.09.003)
- [32] Siebel, E.: *Stahl und Eisen*, 43, 1923, p. 1295.
- [33] Malinowski, J. Z.: *Theoretical and Applied Mechanics*, 14, 1976, p. 347.
- [34] Malinowski, J. Z., Klepaczko, J. R.: *Int. J. of Mech. Sci.*, 28, 1986, p. 381.
[doi:10.1016/0020-7403\(86\)90057-3](https://doi.org/10.1016/0020-7403(86)90057-3)
- [35] Pochhammer, L.: *Journal für die Reine und Angewandte Mathematik*, 81, 1876, p. 324.
- [36] Chree, C.: *Trans. Camb. Phil. Soc.*, 14, 1889, p. 250.
- [37] Chen, S. R., Gray, III, G. T.: In: 2nd International Conference on Tungsten and Refractory. Eds.: Bose, A., Dowding, R. J. Princeton, NJ, Metal Powder Industries Federation 1995, p. 489.
- [38] Duprey, K. E., Clifton, R. J.: In: Shock compression of condensed matter. Eds.: Schmidt, S. C., Dandekar, D. P., Forbes, J. W. Melville, NY, American Institute of Physics 1998, p. 475.
- [39] Kapoor, R. I., Nemat-Nasser, S.: *Metall. Mater. Trans. A*, 31A, 2000, p. 815.
- [40] Lee, B. J., Vecchio, K. S., Ahzi, S. I., Schoenfeld, S.: *Metall. Mater. Trans. A*, 28A, 1997, p. 113.
[doi:10.1007/s11661-997-0087-5](https://doi.org/10.1007/s11661-997-0087-5)
- [41] Vecchio, K. S.: *J. Phys. IV*, 4, 1994, p. 301.